Journal of African Earth Sciences 216 (2024) 105327

Contents lists available at ScienceDirect

Journal of African Earth Sciences

journal homepage: www.elsevier.com/locate/jafrearsci

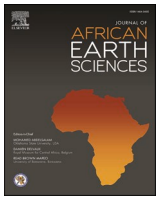

Induced seismicity at the Laúca reservoir, Angola Craton: Focal mechanisms and implications for the stress field in Western Central Africa

Lucas Schirbel [a,b,*], Marcelo Assumpção [a], Francisco António Pereira Neto [c], George Sand França [a]

[a] Universidade de São Paulo, Departamento de Geofísica do IAG/USP, Rua do Matão 1226, Cidade Universitária, 05508-900, São Paulo, SP, Brazil
[b] IPT - Instituto de Pesquisas Tecnológicas do Estado de SP, Av. Prof. Almeida Prado 532, Cidade Universitária, Butantã, 05508-901, São Paulo, SP, Brazil
[c] PRODEL – Empresa Pública de Produção de Electricidade, Município de Belas, Gaveto, Luanda, Angola

ARTICLE INFO

Handling Editor: DR Damien Delvaux

Keywords:
Africa
Angola
Stress field
Focal mechanisms
Reservoir-induced seismicity
Nubian plate

ABSTRACT

We present the first case of reservoir induced seismicity (RIS) ever reported in the Angola Craton, Laúca reservoir. Impoundment of the reservoir began in late 2017 and seismicity started in March 2018 shortly after the water level reached 86 m. Earthquakes continued to be recorded in the following years, with 287 events detected between March/2018 and April/2024. The largest event had magnitude 3.0 ML. The dam is 156 m tall, and the total reservoir volume is 5,044.85 Hm^3. The reservoir area is monitored by two stations, LAUC and ZERO. Seismic data is of high quality, with sharp P- and S-wave arrivals at both stations. We derive a half-space velocity model for the lake area using a composite Wadati diagram and minimization of travel time residuals and locate 90 events with arrivals at both stations. S-to-P converted phases at the surface were used to help constrain hypocentral depths and epicentral locations. We use waveform modeling to determine focal mechanisms for ten events using the program FMNEAR, and invert for the local stress field. We find the faulting regime in the area to be strike-slip and SH_{Max} oriented roughly NE-SW. We compare our results to the broader stress field in western Central Africa and find them to be in agreement with nearby stress determinations from focal mechanisms in the Congo Basin. Our results make an important contribution to the state of knowledge of the stress field in western Central Africa, which can be taken into consideration in future geodynamic models of the Nubian plate as more data is gathered and help further our understanding of stress sources in this region.

1. Introduction

Reservoir Induced Seismicity (RIS) is a well-documented phenomenon, with over 100 cases reported worldwide (Foulger et al., 2018; Gupta, 1992; Wilson et al., 2017). The impounding of water reservoirs significantly changes the normal and shear stresses on pre-existing fault planes through both surface loading and pore pressure changes and serves as a catalyst/trigger for the release of tectonically accumulated stress (Simpson, 1986; Talwani, 1997). There have been dozens of cases of RIS reported in stable continental regions (e.g., Assumpção et al., 2002; Barros et al., 2018; Gupta et al., 1992; Sayão et al., 2020). Intraplate seismicity accounts for only 5% of earth's total seismic moment release and seismicity in stable continental regions accounts for even less, at around 0.5% (e.g., Sandiford and Egholm, 2008). Knowledge of the stress field in intraplate regions is of great importance in understanding plate driving forces and upper mantle dynamics (e.g., Assumpção et al., 2016; Naliboff et al., 2012). Thus, RIS cases in intraplate environments are of great interest to geophysics, as they present an opportunity to map the local stress field in areas where earthquake occurrences are relatively rare, and to test the validity of models derived from other means.

Here we present a new case of RIS, the Laúca reservoir, located in the Kwanza River of the Malanje province of Angola. It is the first known case of RIS reported in the Grand Congo Craton to date. The Grand Congo Craton is a stable continental region formed by the amalgamation of several different cratonic blocks from distinct geological eras (Delvaux et al., 2021). It spans a large area in western Central Africa, from the Atlantic Ocean all the way to the western branch of the East African Rift System in Tanzania. The Angola Craton is one of the many Archean blocks which compose the larger Craton, covering most of southwestern

* Corresponding author. Universidade de São Paulo, Departamento de Geofísica do IAG/USP, Rua do Matão 1226, Cidade Universitária, 05508-900, São Paulo, SP, Brazil.
E-mail addresses: lucas.schirbel@usp.br, lucas.schirbel@alumni.usp.br, lschirbel@ipt.br (L. Schirbel).

https://doi.org/10.1016/j.jafrearsci.2024.105327
Received 9 January 2024; Received in revised form 9 June 2024; Accepted 25 June 2024
Available online 26 June 2024

and central Angola along the Atlantic margin. Laúca reservoir sits atop this cratonic block near its northern borders (Fig. 1).

The Laúca dam is 156 m tall, and the total reservoir volume is 5.045 km^3, which places Laúca in the categories "very deep" and "large volume" (e.g., Baecher and Keeney, 1982). The lake started filling in November 2017, and seismicity began when the water level reached approximately 86 m in March 2018 (Fig. 2). Since then, 287 events have been recorded until April/2024, with the largest event having magnitude 3.0 ML. This event was felt in nearby villages and towns. The maximum magnitude recorded at Laúca and its dam height are compatible with other RIS cases worldwide in that there seems to be no discernible correlation between height and largest magnitude (see Barros et al., 2018).

The reservoir area is characterized by predominantly Paleoproterozoic granitic and Neoproterozoic gneissic rocks (Neto, 2014), with a thin recent sedimentary layer along the Kwanza riverbanks. This places Laúca in category g2/g3 (metamorphic/igneous) of Baecher and Keeney (1982) regarding the geological attributes. Crustal stress data in Angola is scarce due to lack of monitoring in the instrumental era and relatively low overall seismicity.

The lake area is monitored by two seismic stations, LAUC and ZERO, sitting in hard rock outcrops. Both stations operate with broadband (120s–100 Hz) Trillium Compact sensors at a sampling rate of 100 Hz. Station ZERO has been in operation since 2003 in the Capanda dam network, located 40 km upstream from Laúca dam. Impoundment of the older Capanda reservoir in 2002 showed no discernible change in the natural rate of seismicity in the region. Natural earthquakes are known to have occurred in the past around the area where the reservoir is located, with a significant event of magnitude 6.0 M occurring 35 km from the dam in 1914 (Neto et al., 2018). Only three events which could possibly be associated with the operation of the Capanda reservoir were detected in the entire period since it has been in operation, the most recent (and largest) being a magnitude 2.2 ML earthquake in July 2013. No significant induced seismicity around Laúca had been detected in the region monitored by the Capanda network prior to the filling of Laúca dam, and continuous monitoring by at least one seismic station has been ongoing since 2003. LAUC station was installed on May 06, 2018, shortly after seismicity began.

Our goal in this paper is to study the induced seismicity taking place at Laúca reservoir, characterizing the earthquake sequence in terms of both its spatial and temporal distribution as well as relationship to water level variations and to determine focal mechanisms for the largest events in the area, thus obtaining an estimate of the local stress field. We compare these results with theoretical models currently in place for the state of lithospheric stress in the Nubian plate and situate our findings within the broader context of the stress field in western central Africa derived from other focal mechanisms. Laúca is also the first case of induced seismicity to be reported in the wider Congo Craton as well as in Angola and adds an important case to statistical studies of induced seismicity worldwide.

2. Velocity model and epicenters

2.1. Vp/Vs ratio and preliminary Vp determination

P and S arrivals for all events recorded at both stations (90 in total) were manually picked to ensure accuracy. Arrivals are impulsive and sharp (Fig. 3), which allow for precise picking. A Vp/Vs ratio of 1.710 +- 0.003 (Fig. 4) was determined using a composite Wadati Diagram (Kisslinger and Engdahl, 1973). This ratio is typical of felsic rocks, and compatible with the local geology, which is composed mostly of granitic and gneissic rocks.

We start out by deriving a half-space velocity model for the lake area by fixing the Vp/Vs ratio at 1.710 and minimizing travel time residuals.

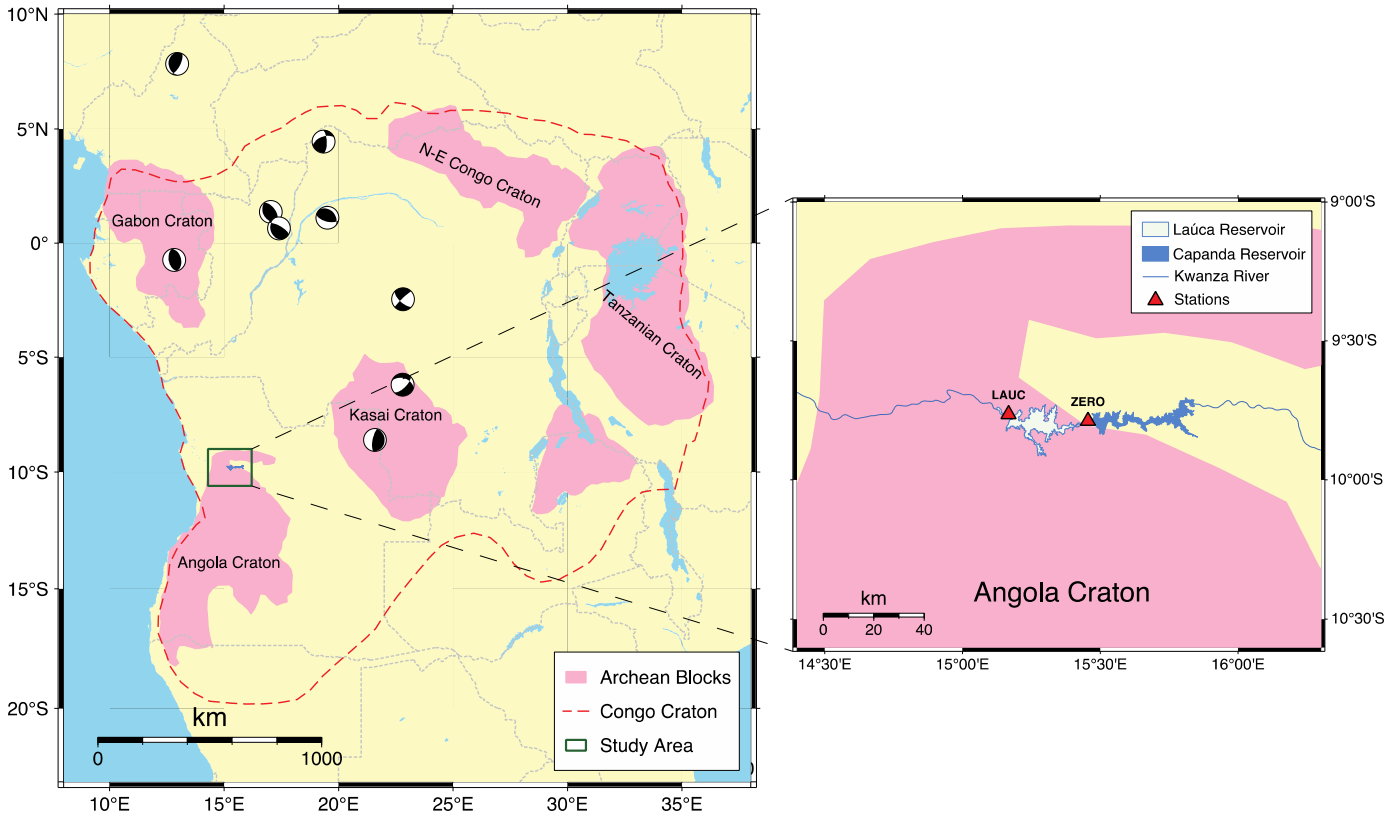

Fig. 1. Regional map indicating the location of the study area within western Central Africa (left panel). The Greater Congo Craton is shown as a dashed red line. Archean blocks, including the Angola Craton, are outlined in pink. Beachballs are focal mechanisms from Delvaux and Barth (2010) in and around the Congo Basin. The study area is shown in detail on the right-side panel. Capanda reservoir is upstream from Laúca and has been in operation since 2003.

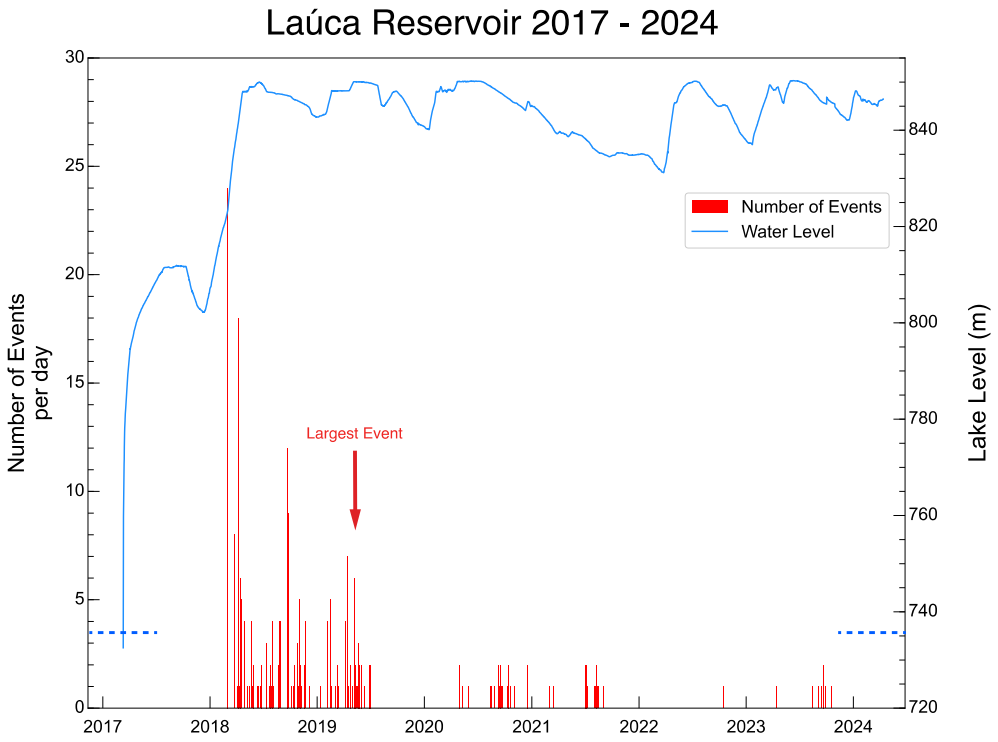

Fig. 2. Event frequency (red bars) x Water level above m.s.l. (blue line) for Laúca reservoir between Jan/2017 and Apr/2024. The dashed line indicates altitude before impoundment. Seismicity started soon after the water height reached 86m in March/2018 and has continued to the present day. The largest event (red arrow) occurred in May/2019 on the northern margin of the lake with magnitude 3.0 ML. All 287 events recorded in the period are shown, including earthquakes recorded at a single station.

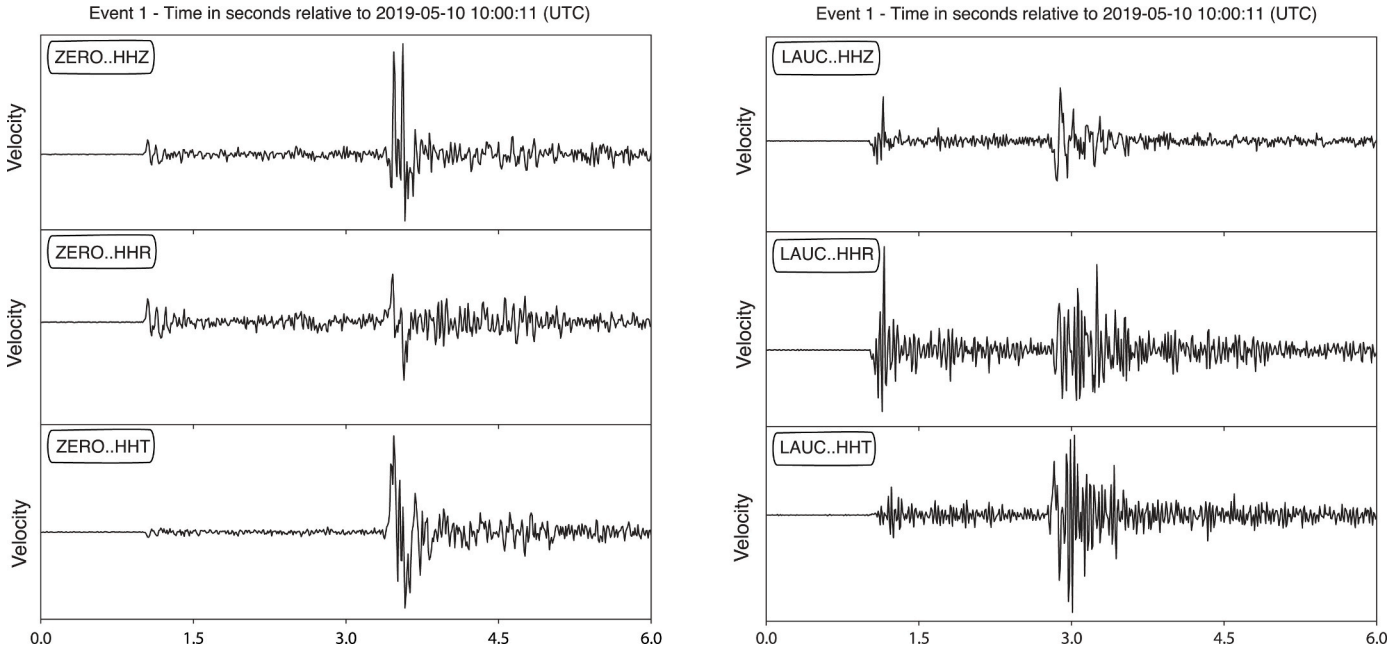

Fig. 3. Unfiltered and rotated (ZRT) seismograms registered at stations ZERO (left) and LAUC (right) for the largest event recorded in the period (3.0 ML) in 2019–05-10 10:00:09 (UTC). Arrivals are impulsive and very sharp at both stations. This clarity in arrivals is observed for most earthquakes registered in the period, even at magnitudes lower than 1.0 MLv.

Since our station coverage is poor, we start by using the program HYPOCENTER (Lienert et al., 1986) to obtain an estimate of the initial location for each event including back azimuths, which were manually measured from particle motion plots for all events. An error of 10° was allowed for all back azimuths, to account for possible uncertainties in station orientation, near surface effects and in the measurements themselves, especially at station LAUC, which is located close to the dam and has a higher noise level. The epicenters obtained from this procedure were then inserted into HYPO71 (Lee and Lahr, 1972) as starting locations for each event to relocate the hypocenters more precisely.

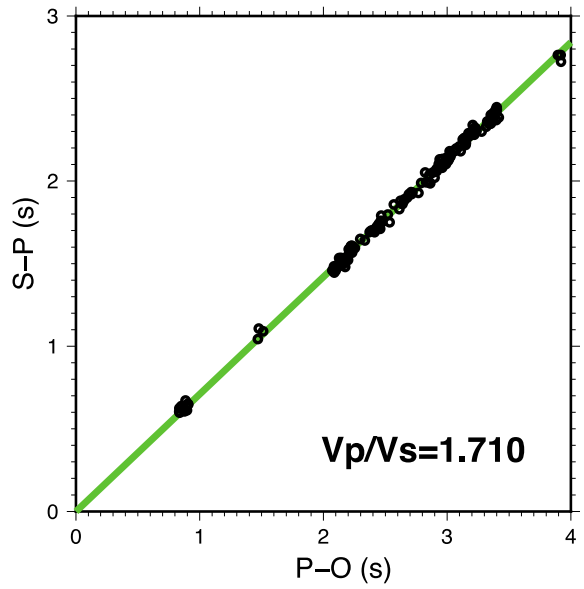

Fig. 4. Composite Wadati diagram for the 90 events with arrivals recorded at both stations. We find a Vp/Vs = 1.710 +- 0.003, which agrees with the local geology. Most of the region sits atop granitic rocks covered by a thin layer of sedimentary rocks in some places.

HYPO71 was chosen to test different depths and to refine locations since it yields a smaller total rms residual in the final solutions when compared to HYPOCENTER. We construct a single half-space layer ranging from 0 km to 15 km with uniform velocity and test Vp values between 5.5 km/s and 6.5 km/s, the expected range of crustal Vp velocities in shields (Christensen and Mooney, 1995).

Depth is not well constrained and was fixed at 2 km, which is the median value obtained when letting it vary. With depth fixed the best preliminary velocity model yields Vp = 6.1 km/s with an RMS residual = 0.007 s.

2.2. Depth estimate using the sPL phase

Depth is poorly constrained for all events given our lack of station coverage. Changes in depth will affect epicentral locations in the N–S direction, and events will move closer to or away from the 2-station line depending on the chosen depth. To deal with this challenge, we adapt the approach of He et al. (2019) to get an independent depth estimate for some events based on the travel time differences of the P and sPL phases, whenever the latter is identifiable. The sPL phase is a well-known SV-to-P conversion at the free surface around the critical angle (Booth and Crampin, 1985). Measuring the travel time difference between the P and sPL arrivals provides an estimate of event depth. We simplify the problem of generating synthetic waveforms presented by He et al. (2019) to that of computing arrival time differences for the P and sPL phases based on a simple half-space model (Fig. 5). The critical angle $ic = \sin^{-1}(Vs/Vp)$ for the lake area is ~35.8°, which means that sPL should start to emerge at epicentral distances greater than about 7–10 km for the range of expected depths at Laúca, i.e., shallow earthquakes (depth <10 km). By varying depth, we can compute theoretical arrival times and compare them to the observed travel time differences for each event.

The sPL method has the advantage of not being as sensitive to epicentral distance as it is to event depth, since the horizontal slowness of both the P and sPL phases are similar at close range. This means that event depth can be constrained even if preliminary locations are off by a relatively large margin. Synthetic seismogram calculations by He et al. (2019) show that even 20 km errors in epicentral locations lead to small (<1 km) errors in the depth estimates using differential travel times for sPL and P for shallow events (<10 km) at local distances. Uncertainties in the velocity model may also introduce systematic bias into the depth estimates, but these are limited to 8% of calculated depth if the error in the velocity model is less than 5%.

Tests using our own adapted model (Fig. 6) show that the difference in estimated depth is less than 1 km for epicentral distances varying between 15 and 30 km for the deepest events (8–10 km), and around 0.5 km for the remaining depths, being practically negligible for the shallowest events (<3 km). At closer epicentral distances (<15 km) the relationship is no longer linear and travel time differences become more pronounced for deeper events. However, none of the events analyzed in our sample where sPL was visible at closer than 15 km from the station are deeper than 3 km. Velocity model changes within the 5% range of the best velocity model led to changes of 0.1s at most for calculated differential travel times at epicentral distances between 15 and 30 km, which result in a depth error of 0.5 km at most for the deepest events. Thus, we can say that although there are hard to quantify uncertainties involved in our epicentral locations and velocity models, our simplified approach agrees with the more sophisticated studies conducted by He

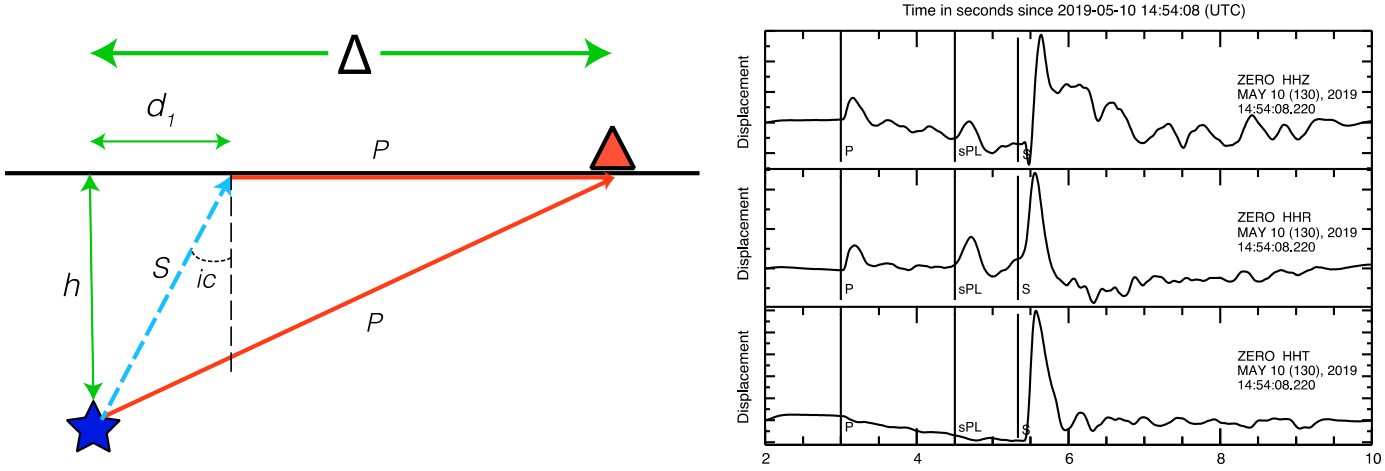

Fig. 5. Left-hand panel: Diagram (adapted from He et al., 2019) showing travel paths for the direct P and sPL arrivals on a simple half-space 1D velocity model from hypocenter (blue star) to station (red triangle). The sPL phase arises from an S wave refracted at the free-surface at the critical angle $ic = \sin^{-1}(Vs/Vp)$. Delta is the epicentral distance, h is hypocentral depth and d_1 is the minimum epicentral distance at which the sPL phase is observable. The difference in travel time between the direct P and sPL arrivals can be used to estimate event depth. Right-hand panel: Identification of the sPL phase on the seismograms of event 6 at ZERO station. Waveforms were low-pass filtered at 2Hz to enhance the sPL arrival.

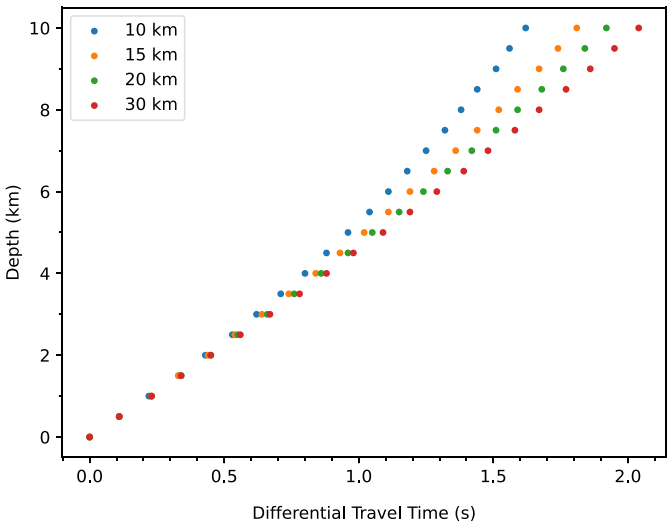

Fig. 6. Differential travel time between the sPL and P crustal phases as a function of depth for different epicentral distances for our adapted half-space model. Each color represents the depth estimate for a certain T (sPL – P) at a particular epicentral distance. The relationship is practically linear for epicentral distances over 15 km, and similar to the results obtained by He et al. (2019) through waveform modeling. Deeper events are more sensitive to errors in epicentral distance, but even large errors in station-event distance lead to reasonably constrained depth estimates.

et al. (2019), and that depth estimates using the sPL phase can be trusted to provide a reasonable estimate of event depth at Laúca.

2.3. Refined Velocity model using sPL depths

We rotate components and filter the events with a low pass filter of 2 Hz to enhance the sPL phase, which is stronger on the radial component. sPL is not visible in all seismograms, and according to He et al. (2019) this visibility varies with station azimuth, radiation pattern (different focal mechanisms) and overall SNR at each station. For the 90 events recorded at both stations, we are able to identify the sPL phase at 20 of them. We estimate depth for these events using our adapted approach, calculating differential travel times in steps of 0.5 km in depth, and choosing the estimated depth based on the nearest measured value of the travel time difference.

We fix the new sPL derived depths for these 20 events and run HYPO71 using the initial HYPOCENTER epicenters again for these events only, and find the new best velocity model to be Vp = 6.3 km/s, with an RMS residual of 0.007 s. It is worth mentioning that the independent depth estimates do not completely overcome the issue of the degree of freedom present in the N–S direction due to lack of station coverage. However, since we have P and S phase readings and back azimuth measurements at both stations for all events, together with an independent depth estimate for this subset, we are able to at least constrain relative locations between events well, given the limitations, and also confirm that lower velocities (<6.3 km/s) lead to much larger RMS residuals when depth is independently determined. Initial locations employing back azimuth measurements also remove the ambiguity between events being located to the north or south of the 2-station line. For Vp models larger than 6.3 km/s, changes in the velocity model can be compensated by moving epicenters farther away from both stations and shifting origin time. However, as mentioned previously, geological constraints on upper crustal velocities in shields set an upper limit for this maximum Vp at 5 km depth at around roughly 6.5 km/s.

2.4. Epicentral distribution

Events in Laúca mainly gather along two faults oriented roughly in the N–S direction, one located on the northern margin of the lake (from here onwards referred to as the main fault) and another across the southeastern margin (the secondary fault). This observed pattern could be due to fault reactivation in the vicinity of the reservoir. Analysis of the temporal distribution of events in the reservoir suggest an epicentral migration of the seismicity away from the center of the reservoir and towards the north on the main fault (Fig. 7), a pattern which is consistent with models of pore pressure diffusion and epicentral migration proposed for reservoirs (e.g., Talwani, 1997). The fact that our station coverage is poor could cause the N–S alignment and migration of seismicity to be an artifact. For example, fixing depth at 2 km for the events where identification of the sPL phase was not possible also means that some events located deeper in the crust might be placed further north, and vice-versa. More data is needed to be sure of this pore pressure diffusion observation and whether pore pressure is also migrating to deeper areas as well as northward on the main fault.

Nevertheless, the sPL derived depths help constrain relative locations along the N–S direction (Fig. 8), showing that the N–S alignment is a robust feature at the main fault, and may be a likely feature in the secondary fault. In fact, the two N–S aligned clusters (main and secondary faults) are parallel to N–S branches of the lake shore, which could indicate geological faults crossing the lake. We can thus conclude that although our data is scarce and absolute epicentral locations have high uncertainties, events in the main fault are not all concentrated in a single cluster but are spread out in the N–S direction, corroborating the hypothesis that the alignment we see is not a smearing artifact arising from the lack of station coverage. This information is useful when attempting to identify fault and auxiliary planes in the focal mechanism solutions.

3. Focal mechanisms and regional stress field

3.1. Focal mechanisms through waveform modeling

We use the program FMNEAR (Delouis, 2014) to determine focal mechanisms through waveform modeling for all events listed in Table 1, which consists of a subset of events with magnitudes larger than 2.0 ML for which the sPL phase was identifiable, and for which the S/N ratio is high enough to be able to obtain good synthetic seismograms. FMNEAR performs a systematic search of focal mechanisms in dip, strike and rake, in predefined angle steps which are then further refined according to the previous best solution. FMNEAR also deals with uncertainties in depth by exploring a range of values for this parameter. Quality criteria are *rms* waveform misfit (which is minimized) and a confidence index. The confidence index is an empirically calibrated scale which serves as an indicator of both the uniqueness and quality of the obtained solution. It is calculated by measuring the "distance" between the lowest *rms* focal mechanism and the other possible solutions discarded during the grid search process. The "distance" between two focal mechanisms is based on the difference between the theoretical P-wave amplitudes for each one of them, calculated over 324 points sampling the focal sphere both in azimuth and take-off angle. Focal mechanisms which predict similar P-wave amplitudes and polarities over the entire focal sphere are considered similar, and vice-versa. Thus, for well-constrained solutions, we expect similar or "close" mechanisms to have a similar *rms* misfit. The solution is thought to be more unique if there are no "distant" focal mechanisms with a *rms* misfit value like that of the best solution. Events where significantly different or "distant" focal mechanisms yield similar *rms* misfits are considered unreliable and are assigned a lower confidence index. The confidence index also considers the number of components used and the absolute value of the calculated *rms* misfit, with more components and a lower overall *rms* yielding a higher value. Confidence indexes below 70% are not considered robust, and those above 80% are considered well established, assuming hypocentral locations are correct. FMNEAR also employs underweighting of stations which are closer than 20 km to the epicenter. This is useful in dealing

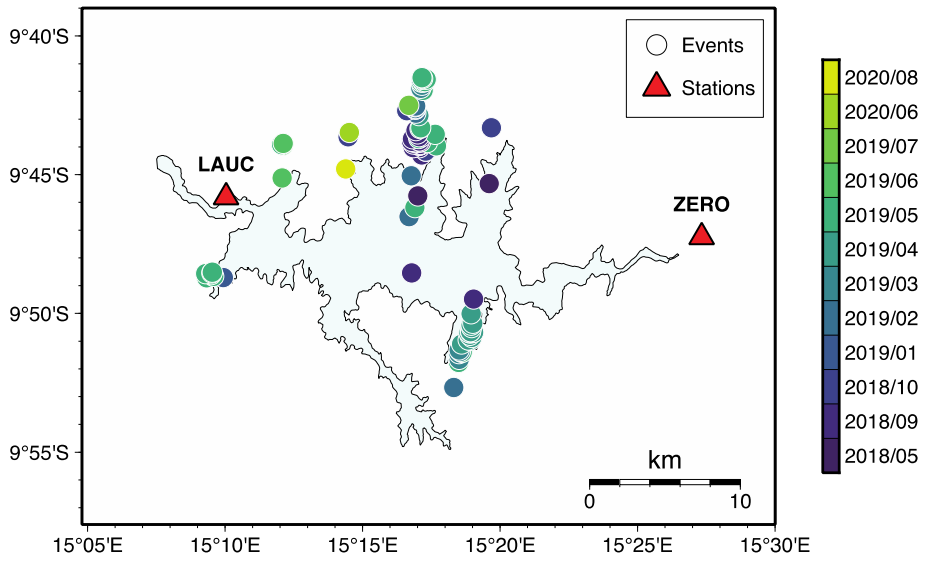

Fig. 7. Final event locations (colored circles) using the best velocity model for the lake area (Vp = 6.3 km/s, Vp/Vs = 1.710). The events shown here are those recorded at both stations (LAUC and ZERO). Epicentral locations were determined using the sPL depths for events where those were available and by fixing depth at 2 km for the remaining events. Most events cluster along two faults roughly oriented in the N–S direction. The color bar indicates the year and month in which each event occurred. We see a tentative outward migration pattern over time on the main fault, located at the northern edge of the reservoir, which suggests that it is being reactivated as pore pressure diffuses. On the southern fault, events happen almost all on the same month, and no clear migration pattern is discernible.

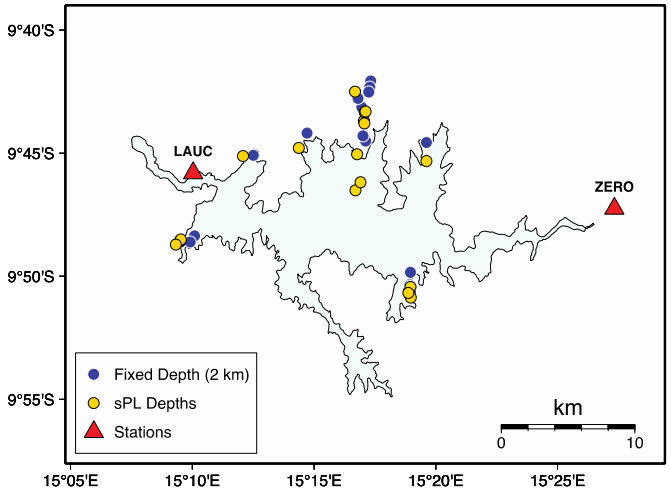

Fig. 8. Event locations with depth fixed at 2 km (blue circles) and after fixing depth according to the best sPL estimates (yellow circles). Events located on the main fault are more spread out after relocation with the estimated depths and delineate a N–S trend. On the secondary fault, events also seem to follow a N–S trend, but since they are closer together, it is not possible to be certain.

Table 1
Events chosen for focal mechanism determination. Seven events are located on the northernmost fault (main fault), two on the southeast fault (secondary fault) and one to the west of the main fault, near LAUC station and close to the dam wall.

Origin Time (UTC)	Event ID	Latitude	Longitude	Magnitude (ML)	Fault
2019-05-10 10:00:09	1	−9.7218	15.2853	3.0	Main fault
2019-02-05 05:17:30	2	−9.7752	15.2782	2.5	Main fault
2019-02-16 23:21:26	3	−9.7507	15.2795	2.3	Main fault
2018-09-22 18:52:23	4	−9.7298	15.2843	2.1	Main fault
2019-05-10 14:54:07	5	−9.7698	15.2817	2.6	Main Fault
2019-04-13 19:22:08	6	−9.8448	15.3145	2.2	Secondary fault
2019-04-14 13:10:32	7	−9.8405	15.3158	2.0	Secondary fault
2019-05-10 10:19:07	8	−9.7223	15.2848	2.3	Main Fault
2019-06-11 17:29:53	9	−9.7520	15.2013	2.2	Neither
2019-05-10 09:59:35	10	−9.7283	15.2840	2.1	Main Fault

with possible large travel path errors arising from epicentral uncertainties at close distances.

We use the same velocity model used for the hypocentral determinations (Vp = 6.3 km/s, Vp/Vs = 1.710), with attenuation coefficients Qp = 200 and Qs = 100. We allow the program to test different depths close to the best estimated sPL depth (Table 2) to consider possible errors arising from uncertainties in the velocity model and epicentral distances. Band-pass filters were chosen on a case-to-case basis through trial and error, and a bandpass filter of 0.4–0.9 Hz proved to be the best choice for most events. Filtering is necessary to remove high frequency noise content and small structure effects along the event-receiver path, which lead to low-quality solutions. Focal mechanism parameters are shown in Table 3. Confidence indexes are above or at 70% for all computed solutions. Four events have confidence indexes above 80%. Using the sPL depths, rather than depth at fixed 2 km, leads to better agreement between observations and synthetics. An example of waveform fitting for event 1 is shown in Fig. 9.

We explore a suite of depths by calculating focal mechanisms in steps of 1 km for each event, varying depth from 1 to 15 km (Fig. 10). Event 1 and events 6 through 10 all show a very pronounced *rms* minimum around the chosen depth. For these events, solutions are robust around the chosen depth, with little variation in the focal mechanisms. For event 2, shallow depth solutions have similar *rms*, but focal mechanism changes are not significant between them. Events 3 and 4 also show a minimum around the chosen depth and stable focal mechanisms around the lowest *rms* values, but this minimum is not as pronounced as in the other events. Event 5 is the only focal mechanism where solutions are not stable around the local minimum. This reflects the low confidence index (70%) for this event. The solutions with lowest *rms* are those at 8

Table 2
Depth estimates from sPL travel times for events 1 to 10. The sPL phase was visible at different degrees of confidence for all events listed below at station ZERO only, and tentatively for event 4 at station LAUC.

	Estimated Depth	$T_{sPL} - T_P$ (ZERO)	$T_{sPL} - T_p$ (LAUC)
Event 1	7.5 km	1.49 s	–
Event 2	6.0 km	1.26 s	–
Event 3	6.0 km	1.23 s	–
Event 4	3.0 km	0.63 s	0.54 s
Event 5	7.5 km	1.49 s	–
Event 6	4.0 km	0.80 s	–
Event 7	3.0 km	0.63 s	–
Event 8	7.0 km	1.45 s	–
Event 9	3.5 km	0.72 s	–
Event 10	7.5 km	1.49 s	–

Table 3
FMNEAR inversion parameters and best fault plane solution for each event. Discrimination between fault and auxiliary planes for each solution was made based on the epicentral distribution of the events. Selected depth was allowed to vary slightly from the sPL determined depth to account for possible errors in the chosen velocity model. The listed nodal plane refers to the inferred fault plane for all events except event 9.

	Strike (°)	Dip (°)	Rake (°)	Selected Depth (km)	R.M.S.	Confidence Index (%)
Event 1	13.1	87.7	140.0	7.0	0.304	87
Event 2	178.0	68.7	174.6	4.0	0.242	77
Event 3	175	66.6	−180	5.0	0.404	78
Event 4	185	45	143.6	3.0	0.501	70
Event 5	209.7	70.7	−125.7	8.0	0.456	74
Event 6	25	80	−165	4.0	0.388	89
Event 7	25	85	−160	3.0	0.447	81
Event 8	204.8	59.3	−131.6	7.0	0.409	85
Event 9	50	60	−124.6	3.0	0.569	77
Event 10	200.5	67.3	−135.8	8.0	0.469	77

km and 9 km. The difference in *rms* between the two solutions in negligible, and we choose the focal mechanism at 8 km depth in this case since this event is part of a seismic sequence happening on the same day as events 1, 8 and 10, and this focal mechanism is more similar to those, which are better constrained, than to the one at 9 km depth. Overall, the depth with the lowest *rms* and best solution agrees with the sPL estimated depth within 1.5 km for all events except event 2, where the chosen depth is 2 km shallower than the estimated depth.

All focal mechanisms except event 9 had one of the nodal planes trending in the general direction of the N–S and NNE-SSW epicentral distribution of the main and secondary faults, albeit with some slight variations in strike, trending towards the NE direction for most events located on the main fault. We take these nodal planes to be the fault planes. In the case of event 9, it is not possible to discern the fault and auxiliary planes. All events located on the faults show right-lateral strike-slip faulting with varying smaller reverse or normal components (Fig. 11). Some event pairs show very similar mechanisms, as we can see by comparing events 1, 5, 8 and 10 (all happening on the same day and presumably part of the same earthquake sequence), events 2 and 3 (geographical proximity and waveform similarity) and events 6 and 7 (both located on the secondary fault). The fault and auxiliary plane variations across mechanisms which happen on the same fault, and even on the same day (thought to be part of the same earthquake sequence) reflect the uncertainties present in the mechanisms given our data limitation and confidence indexes. Auxiliary plane uncertainties seem to be more pronounced than those for the chosen fault planes, in both strike and dip. Event 9, the only one not located on either fault, is an oblique normal faulting mechanism with a strike-slip component, and one fault plane trending in the general direction of the alignment of the tributaries of the Kwanza River, as inferred from the flooding pattern of the reservoir.

Fig. 11 also illustrates a possible seismotectonic scheme for the lake area. The distribution of focal mechanisms suggests two right-lateral strike-slip faults, with the main fault at the northernmost edge of the reservoir striking N–S and the secondary fault striking NNE-SSW. Most fault planes as identified using our previous criteria of epicentral distribution are steeply dipping. Focal mechanisms vary between pure strike-slip to oblique strike-slip with normal faulting components, and one mechanism displays a reverse component. Previous fault mapping in the area prior to impoundment had identified a few surface faults, probably strike-slip, across the course of the Kwanza River striking predominantly in the NW-SE direction. Although faults on the surface seldom match faults at depth from focal mechanisms, our epicentral distribution indicates that some of these strike-slip faults are possibly being reactivated by the filling of the reservoir.

3.2. Stress inversion from focal mechanisms

We estimate the orientation of the principal stresses in this area by inverting the ten focal mechanisms.

We assume the crustal stress field at Laúca to be uniform, and that the observed slip direction has the same direction as the shear stress on the fault planes. Principal stresses were constrained to the horizontal and vertical directions, partly due to the small number of focal mechanisms for a full 3D inversion, but also due to the free surface being a principal plane. We employ the method of Michael (1984, 1987) to perform a grid search of the principal stress directions S1, S2 and S3 and also of the shape factor $\phi = \frac{(S2-S3)}{(S1-S3)}$ which minimize the observed difference between the calculated and observed rakes. Fault planes were chosen based on the observed epicentral distribution for events on the main and secondary faults. For event 9 no fault plane was chosen, and the program is allowed to choose the fault plane that minimizes rake misfit. We search the focal sphere in steps of 1° for the stress directions and 0.1 for the shape factor. Fig. 12 shows the best fit to the observed rakes. The maximum and minimum stresses were both found to be horizontal, with S1 (SH_{MAX}) oriented at 237°, S2 vertical, and S3 (SH_{MIN}) oriented at 147°, with an average misfit of 21.3° for rake on the fault planes and a maximum misfit of 43°. This indicates a strike-slip faulting regime. The shape factor $\phi = 0.70$ indicates that the magnitude of the confining stress S2 is closer to S1 than to S3. Not choosing the fault planes for events 6 and 7 on the secondary fault does not significantly alter the results. The average angle between the calculated SH_{MAX} direction and the fault planes is 38° ± 16°, with the minimum being 7° and the maximum 62°. Although geomechanical expectations are that SH_{MAX} be within ±30° of the fault planes in the case of brittle fracture of homogeneous materials, the only restrictions upon SH_{MAX} for shallow earthquakes reactivating weak failure planes is that SH_{MAX} be oriented anywhere within the P-wave dilatational quadrant (McKenzie, 1969).

The small number of focal mechanisms used for the stress inversion as well as the high degree of similarity between some of them makes the stress inversion not as well constrained as in the ideal case, where a plethora of different focal mechanisms with varying parameters is desired. More mechanisms in different parts of the reservoir would likely improve solutions, but are difficult to obtain for events with magnitude lower than 2.0 ML. Nevertheless, a stress inversion in this case is still a better estimator of the direction of SH_{MAX} than simply taking the average orientation of the direction of the P axis for each focal mechanism. Although a small set of local focal mechanisms is not enough to determine the stress field on a regional scale, stress data for this area of the world is scarce. Thus, any estimate of SHmax for this region, however limited, still makes an important contribution to the state of knowledge of the stress field along the Atlantic margin and could be used as a first approximation to constrain geodynamical models and to better understand tectonics. Laúca is also the first case of induced seismicity to

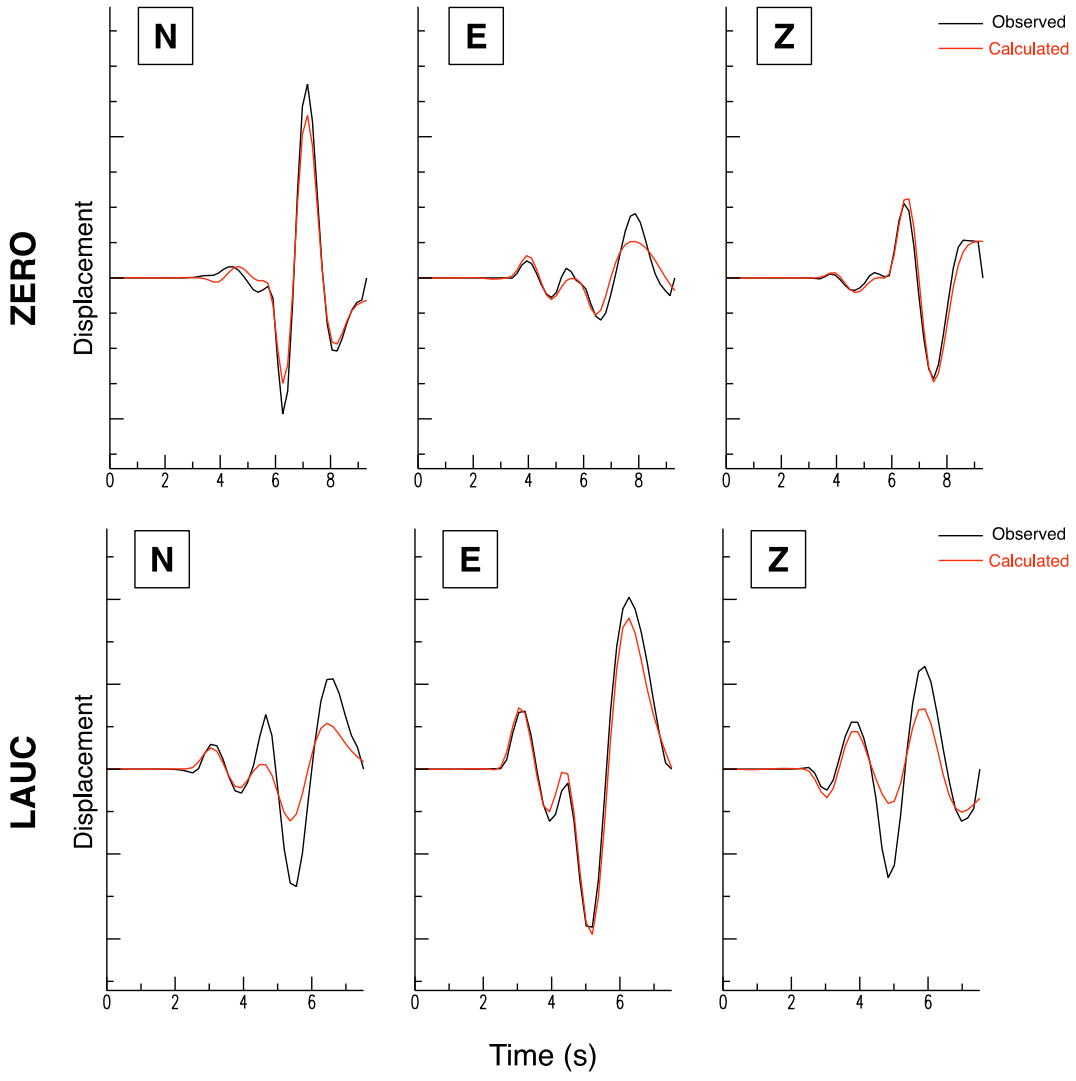

Fig. 9. Synthetic (red lines) and observed (black line) seismograms for event 1 at stations ZERO (top panel) and LAUC (bottom panel). Components are, from left to right: North, East, and Vertical. Waveforms were filtered in the 0.2–0.7 Hz range. Observed and computed seismograms show improved agreement after relocation using the new depths determined from the sPL phases.

be reported in the wider Congo Craton and in Angola, adding an important case to statistical studies of induced seismicity worldwide.

4. Discussion

4.1. Inducing attributes and seismicity patterns

Initial statistical analyses (Baecher and Keeney, 1982) demonstrated that depth is the main attribute related to reservoir induced seismicity. Very deep reservoirs (over 150 m, such as Laúca) had a probability of causing earthquakes estimated at about 27%. Volume was the second most important attribute. Large reservoirs (more than 1.2 km^3), such as Laúca, had a probability of 21%. Analysis of 26 cases of RIS in Brazil, a similar stable continental region, by Barros et al. (2018) showed that reservoirs about 150 m deep would have 60%–70% probability of RIS. Considering only the volume, large reservoirs (between 1.0 and 10 km^3) had about 26% chance of producing seismicity.

Tectonic regime also influences the likelihood of RIS (Baecher and Keeney, 1982); reservoirs in strike-slip regimes are more prone to induce earthquakes, as in the Laúca case. Probabilities were estimated at around 18% for such reservoirs, compared with those in extensional or compressional regimes (about 11%). Therefore, Laúca reservoir seems to be a typical case for inducing earthquakes both for being very deep and large as well as for the strike-slip regime.

Regarding geological attributes, the preliminary analyses of Baecher and Keeney (1982) suggested a slightly higher probability for reservoirs in predominantly sedimentary basins (16%) compared with metamorphic and igneous geology (about 11% each). On the other hand, the analyses of the 26 Brazilian cases (Barros et al., 2018; Sayão et al., 2020) suggested that reservoirs in metamorphic or igneous basements have slightly higher probabilities (5–6 %) compared to 4 % of those in sedimentary basins. Clearly, geology is not a very important attribute in estimations of RIS probabilities. The Laúca case may help improve future studies of the main contributing factors for reservoir induced seismicity.

In terms of the classification by Simpson (1986) and Talwani (1997), seismicity at Laúca seems to be initial only, with levels of seismic activity decreasing continuously since filling and trending back towards pre-impoundment levels, with no discernible pattern observed following water level variations after 2021, which indicate a lack of possible protracted or delayed seismicity. The observed seismicity pattern at Laúca is unusual, with events distributed along what seem to be pre-existing faults instead of the more common clustered or widespread patterns. In most cases of RIS, epicenters seem to be scattered in many

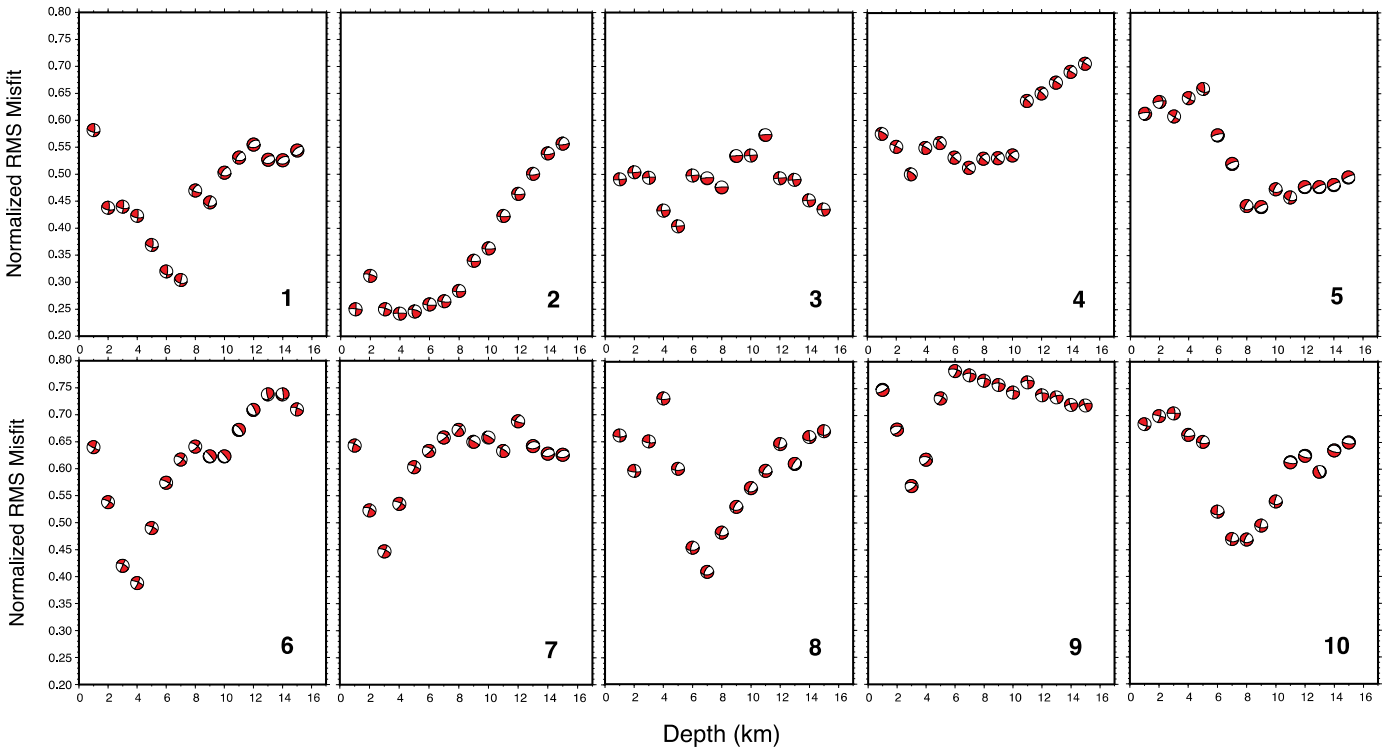

Fig. 10. Evaluation of best RMS misfit x depth for FMNEAR events. Event number is indicated on the bottom right corner. Depths between 1 and 15 km were tested for all events. Normalized RMS misfit scales are the same for all events and vary between 0.2 and 0.8. Depth is shown in km beneath each plot.

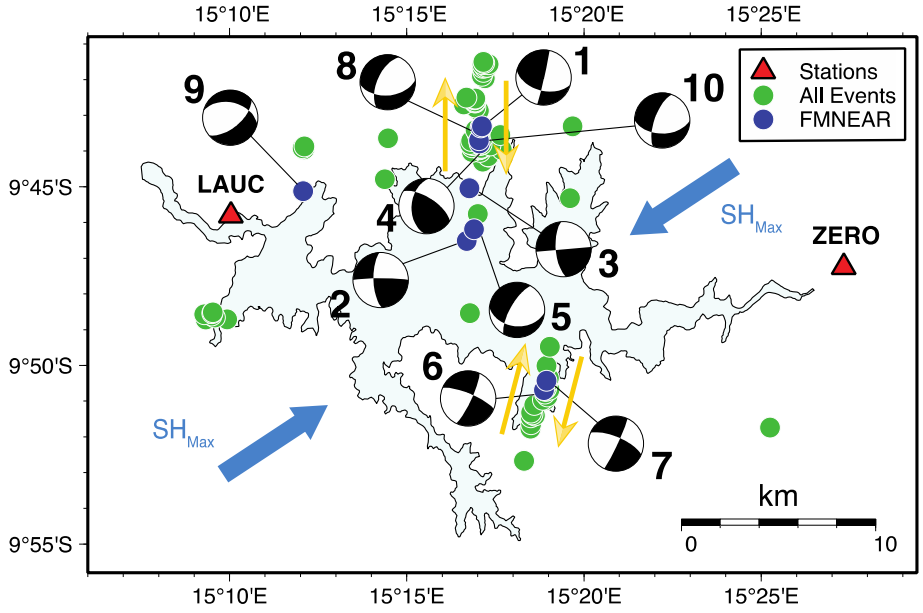

Fig. 11. Focal mechanisms superimposed on the epicentral distribution around the lake area. Epicentral locations were determined using the sPL depths for events where those were available and by fixing depth at 2 km for the remaining events. Blue circles show the epicenters of events for which focal mechanisms were computed using FMNEAR. Fault motion in the lake area is predominantly right-lateral strike-slip with a normal component for most events, which aligns well with the observed faults delineated by the epicenters (blue and green circles). Yellow arrows show possible fault motion inferred from the focal mechanisms.

different faults or fractures and do not clearly align along a few faults (e.g., Gupta, 1992). In the stable continental region of Brazil, for example, most cases show epicenters spread around the reservoir area, or clustered in some areas, without a clear association with well-defined faults, such as Cajuru and Sobradinho (Gupta, 1992), Tucuruí and Nova Ponte (Assumpção et al., 2002; Raza et al., 2023), Serra da Mesa, Itapebi and Funil (Barros et al., 2018), Irapé (Silva et al., 2014), and Castanhão (Castro Nunes et al., 2011). The only case with epicenters clearly aligned along a few faults is the Assu reservoir in NE Brazil (Ferreira et al., 1995). In this case, three separate faults were identified and had strike-slip motion, like the Laúca reservoir.

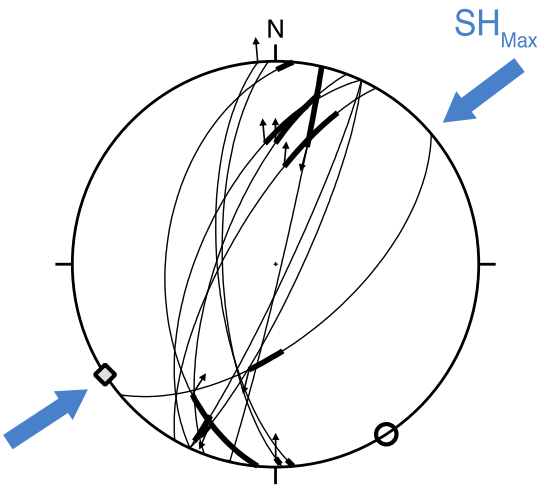

Fig. 12. Stress tensor inverted from the ten focal mechanisms in the lake area. Stresses were constrained to the vertical and horizontal directions because of the free surface. The gray diamond indicates S1 (SH_{Max}) and the open circle S3 (SH_{Min}), the maximum and minimum compressive stresses, respectively. Blue arrows show the SH_{Max} direction. Fault planes are represented by thin lines, and arrows represent the observed slip vectors on fault planes. Thick line segments show the misfit between the observed and calculated rakes.

4.2. Stress field

The African stress field is still largely unmapped through focal mechanisms because of the overall low seismicity in intraplate regions and lack of adequate network coverage in many areas. We would expect the entire African continent to be in compression given that it is surrounded (except in the north) by spreading ridges. This is not what is observed. Most of the African continent is in extension, and the first order stress field caused by plate boundary forces arising from spreading ridges, continental collisions and basal drag cannot explain this. Thus, other sources of stress must be at play.

Numerical modeling by Coblentz and Sandiford (1994) predicted that the ambient state of stress in the continental Nubian plate was extensional and could be explained mostly by gravitational potential energy gradients arising from lateral density variations in the lithosphere, in good agreement with the available stress data at the time. Their model predicted extensional tectonics for regions above 650m in altitude (the continental mean), which would include Laúca (located at 855m). They do note, however, that model sensitivity is limited to long wavelengths and that P axes of focal mechanisms along West Africa vary greatly, suggesting that local or regional sources of stress might dominate the stress field in this region.

Mahatsente and Coblentz (2015) evaluated how ridge-push forces contribute to the state of stress of the Nubian-Somalian plate. They found that stresses originating from the gravitational potential energy of the ridges could be transmitted into the continental areas of the plate and predicted primarily strike-slip or extensional tectonics for continental regions above ~500m, in agreement with our findings. Their predicted SH_{MAX} direction around the area where Laúca dam is located is N–S, while ours is NE-SW. It should be noted, however, that the sensitivity of their model is also limited to large scale features spanning at least a few hundred kilometers. Therefore, the NE-SW compression we observe in our stress inversion could have arisen from other contributing factors such as local or regional stress sources, e.g., potential energy differences between cratonic lithospheric roots and the surrounding regions (Zoback and Mooney, 2003).

Further work by Delvaux and Barth (2010) inverting for stress using focal mechanisms over the Nubian and Somalian plates show that the stress field in Africa varies greatly between different regions. Their results in the Congo Basin and adjacent areas found that this part of the continent is in compression, with SH_{MAX} oriented in the E-W direction and most earthquakes showing either strike-slip or reverse faulting. Nkodia et al. (2022) used more focal mechanisms and found SH_{MAX} oriented in the ENE-WSW direction for the continental interior in that region. These results disagree with Coblentz and Sandiford (1994), who predict a neutral state of stress for this area, highlighting that regional sources of stress are not captured in large scale simulations, and play an important role in faulting regimes. Most of the focal mechanisms used in these analyses are thousands of kilometers away from Laúca, emphasizing the importance of the contribution our events can make in this area. Despite the small number of focal mechanisms, our estimates of stress regime and SHmax orientation seem to agree with the general trend in the region, which leads us to believe that they are useful as a first approximation.

Topography seems to play an important role in the second order stress field over western Central Africa, and as we move south the faulting regime shifts from reverse at the Congo Basin to strike-slip at Láuca and then from strike-slip to normal in Northern Namibia, with SH_{MAX} also changing from E-W to NE-SW to NNW-SSE (Delvaux and Barth, 2010; Heidbach et al., 2018). Variations in elevation along the Angolan and Namibian territories could explain these changes. Spreading stresses from the passive margin are another possibility. Thus, the interplay between the first and second order stress field (presumably from gravitational spreading) could explain the SW-NE direction we found for SH_{MAX} and the strike-slip faulting regime at Laúca. Obtaining focal mechanisms farther south at higher altitudes in Angola both near the continental margin as well as the continental interior would allow us to better test this hypothesis and study how the interplay between gravitational spreading due to topography and E-W compression from plate-wide forces affect the stress field in this area.

Overall, more stress data from focal mechanisms in the region is needed to better define the stress field over different parts of the elevated continent and improve our understanding of the sources of the observed stresses in this part of Africa.

5. Conclusions

Geodynamical models need to consider the stress field of the interior of continents if they hope to explain plate motion and tectonic evolution. In stable continental regions well-recorded events for which focal mechanisms can be obtained are a rare find. In this respect, induced seismicity, when recorded by a local network, such as in Laúca, presents a great opportunity to study regional tectonics and the local stress field.

Events at Láuca are generally small (magnitudes$\leq$3.0 ML), but very clearly recorded. We tackle the challenge of working with only two seismic stations by employing different methods to constrain epicentral locations. Back azimuth measurements along with independent depth estimates using S-to-P converted phases allow us to distinguish between events located to the north or south of the 2-station line and to restrict their epicentral locations in the N–S direction. Epicentral distributions show an alignment of seismicity in the N–S direction at the northern portion of the reservoir which aids in the identification of fault planes in the focal mechanism solutions. Seismicity at Laúca seems to be returning to background levels 6 years after impoundment, displaying a sharp decline in number of events and not responding to seasonal water level variations.

We characterize the seismicity induced by the reservoir and obtain focal mechanisms for ten events, which suggest a strike-slip faulting regime in the area, with NE-SW deviatoric compression. Our stress tensor inversion falls in line with previous work done in the region, and hints at possible second order stress field contributions being present in Angola. Even with our limitations owing to the very small amount of data, we nonetheless provide a first rough estimate of the stress field along the continental margin in Angola, serving as a new constraint for future geodynamic modeling in the Nubian plate, in a region where no data was previously available, and add a new well documented case of

RIS to the worldwide database.

CRediT authorship contribution statement

Lucas Schirbel: Writing – review & editing, Writing – original draft, Visualization, Validation, Software, Methodology, Investigation, Formal analysis, Data curation, Conceptualization. **Marcelo Assumpção:** Writing – review & editing, Validation, Supervision, Software, Methodology, Investigation, Conceptualization. **Francisco António Pereira Neto:** Writing – review & editing, Validation, Resources, Data curation. **George Sand França:** Writing – review & editing, Validation.

Declaration of competing interest

The authors declare that they have no known competing financial interests or personal relationships that could have appeared to influence the work reported in this paper.

Data availability

The authors do not have permission to share data.

Acknowledgments

We thank PRODEL-EP and Capanda Hydroelectric Company for allowing publication of the Laúca case, and IPT for the allotted hours to carry out this work. GSF thanks CNPq PQ grants.

The Capanda Dam Monitoring Dept (PRODEL-EP) installed the stations and carried out preliminary analyses. PRODEL – EP is responsible for the operation of all hydroelectric power plants in Angola, including Laúca.

References

Assumpção, M., Marza, V., Barros, L., Chimpliganond, C., Soares, J.E., Carvalho, J., et al., 2002. Reservoir-induced seismicity in Brazil. The Mechanism of Induced Seismicity, pp. 597–617.

Assumpção, M., Dias, F.L., Zevallos, I., Naliboff, J.B., 2016. Intraplate stress field in South America from earthquake focal mechanisms. J. S. Am. Earth Sci. 71, 278–295.

Baecher, G.B., Keeney, R.L., 1982. Statistical examination of reservoir-induced seismicity. Bull. Seismol. Soc. Am. 72 (2), 553–569.

Barros, L.V., Assumpção, M., Ribotta, L.C., Ferreira, V.M., de Carvalho, J.M., Bowen, B. M., Albuquerque, D.F., 2018. Reservoir-triggered seismicity in Brazil: statistical characteristics in a midplate environment. Bull. Seismol. Soc. Am. 108 (5B), 3046–3061.

Booth, D.C., Crampin, S., 1985. Shear-wave polarizations on a curved wavefront at an isotropic free surface. Geophys. J. Int. 83 (1), 31–45.

Castro Nunes, B.I.D., do Nascimento, A.F., Ferreira, J., Assumpção, M., Menezes, E.A.D., 2011. Reservoir-induced seismicity at Castanhão (NE Brazil). In: 12th International Congress of the Brazilian Geophysical Society & EXPOGEF, Rio de Janeiro, Brazil, 15–18 August 2011. Society of Exploration Geophysicists and Brazilian Geophysical Society, pp. 1404–1407.

Christensen, N.I., Mooney, W.D., 1995. Seismic velocity structure and composition of the continental crust: a global view. J. Geophys. Res. Solid Earth 100 (B6), 9761–9788.

Coblentz, D.D., Sandiford, M., 1994. Tectonic stresses in the African plate: constraints on the ambient lithospheric stress state. Geology 22 (9), 831–834.

Delouis, B., 2014. FMNEAR: determination of focal mechanism and first estimate of rupture directivity using near-source records and a linear distribution of point sources. Bull. Seismol. Soc. Am. 104 (3), 1479–1500.

Delvaux, D., Barth, A., 2010. African stress pattern from formal inversion of focal mechanism data. Tectonophysics 482 (1–4), 105–128.

Delvaux, D., Maddaloni, F., Tesauro, M., Braitenberg, C., 2021. The Congo Basin: stratigraphy and subsurface structure defined by regional seismic reflection, refraction and well data. Global Planet. Change 198, 103407.

Ferreira, J.M., Oliveira, R.T.D., Assumpção, M., Moreira, J.A., Pearce, R.G., Takeya, M. K., 1995. Correlation of seismicity and water level in the Açu reservoir—an example from northeast Brazil. Bull. Seismol. Soc. Am. 85 (5), 1483–1489.

Foulger, G.R., Wilson, M.P., Gluyas, J.G., Julian, B.R., Davies, R.J., 2018. Global review of human-induced earthquakes. Earth Sci. Rev. 178, 438–514. https://doi.org/10.1016/j.earscirev.2017.07.008.

Gupta, H.K., 1992. Reservoir Induced Earthquakes. Elsevier, p. 364pp.

He, X., Zhang, P., Ni, S., Zheng, W., 2019. Resolving focal depth in sparse network with local depth phase sPL: a case study for the 2011 mineral, Virginia, earthquake sequence. Bull. Seismol. Soc. Am. 109 (2), 745–755.

Heidbach, O., Rajabi, M., Cui, X., Fuchs, K., Müller, B., Reinecker, J., et al., 2018. The World Stress Map database release 2016: crustal stress pattern across scales. Tectonophysics 744, 484–498.

Kisslinger, C., Engdahl, E.R., 1973. The interpretation of the Wadati diagram with relaxed assumptions. Bull. Seismol. Soc. Am. 63 (5), 1723–1736.

Lee, W.H.K., Lahr, J.C., 1972. HYPO71: a computer program for determining hypocenter, magnitude, and first motion pattern of local earthquakes. US Department of the Interior. Geological Survey, National Center for Earthquake, Research, p. 100.

Lienert, B.R., Berg, E., Frazer, L.N., 1986. HYPOCENTER: an earthquake location method using centered, scaled, and adaptively damped least squares. Bull. Seismol. Soc. Am. 76 (3), 771–783.

Mahatsente, R., Coblentz, D., 2015. Ridge-push force and the state of stress in the Nubia-Somalia plate system. Lithosphere 7 (5), 503–510.

McKenzie, D.P., 1969. The relation between fault plane solutions for earthquakes and the directions of the principal stresses. Bull. Seismol. Soc. Am. 59 (2), 591–601.

Michael, A.J., 1984. Determination of stress from slip data: faults and folds. J. Geophys. Res. Solid Earth 89 (B13), 11517–11526.

Michael, A.J., 1987. Use of focal mechanisms to determine stress: a control study. J. Geophys. Res. Solid Earth 92 (B1), 357–368.

Naliboff, J.B., Lithgow-Bertelloni, C., Ruff, L.J., de Koker, N., 2012. The effects of lithospheric thickness and density structure on Earth' s stress field. Geophys. J. Int. 188 (1), 1–17.

Neto, F.A.P., França, G.S., Condori, C., Sant'Anna Marotta, G., Chimpliganond, C.N., 2018. Angola seismicity. J. Seismol. 22, 1113–1126.

Neto, Francisco António Pereira, 2014. Estudo da sismicidade natural de Angola e desencadeada no Médio Kwanza. 2014. xiv, 134 f., il. Dissertação. Mestrado em Geociências Aplicadas) - Universidade de Brasília, Brasília.

Nkodia, H.M.D.V., Miyouna, T., Kolawole, F., Boudzoumou, F., Loemba, A.P.R., Bazebizonza Tchiguina, N.C., Delvaux, D., 2022. Seismogenic fault reactivation in western Central Africa: insights from regional stress analysis. G-cubed 23 (11), e2022GC010377.

Raza, H., Kivi, I.R., França, G.S., Vilarrasa, V., 2023. Reservoir impoundment-triggered seismicity in Brazil: the case of M4. 0 Nova Ponte earthquake. Sci. Rep. 13 (1), 22226.

Sandiford, M., Egholm, D.L., 2008. Enhanced intraplate seismicity along continental margins: some causes and consequences. Tectonophysics 457 (3–4), 197–208.

Sayão, E., França, G.S., Holanda, M., Gonçalves, A., 2020. Spatial database and website for reservoir-triggered seismicity in Brazil. Nat. Hazards Earth Syst. Sci. 20 (7), 2001–2019.

Silva, G.F.D., Araújo Filho, J.O.D., Huelsen, M.G.V., Chimpliganond, C.N., França, G.S., 2014. Influence of Brazilian structures on the reservoir induced seismicity case of Irapé hydroelectric plant, minas gerais, Brazil. Braz. J. Genet. 44, 375–386.

Simpson, D.W., 1986. Triggered earthquakes. Annu. Rev. Earth Planet Sci. 14 (1), 21–42.

Talwani, P., 1997. On the nature of reservoir-induced seismicity. Pure Appl. Geophys. 150, 473–492.

Wilson, M.P., Foulger, G.R., Gluyas, J.G., Davies, R.J., Julian, B.R., 2017. HiQuake: the human-induced earthquake database. Seismol Res. Lett. 88 (6), 1560–1565.

Zoback, M.L., Mooney, W.D., 2003. Lithospheric buoyancy and continental intraplate stresses. Int. Geol. Rev. 45 (2), 95–118.